

# A Gas-Phase Migration Strategy to Synthesize Atomically Dispersed Mn-N-C Catalysts for Zn–Air Batteries

Qingyan Zhou, Jiajun Cai, Zhen Zhang, Rui Gao, Bo Chen, Guobin Wen, Lei Zhao,\* Yaping Deng, Haozhen Dou, Xiaofei Gong, Yunlong Zhang, Yongfeng Hu, Aiping Yu, Xulei Sui,\* Zhenbo Wang,\* and Zhongwei Chen\*

Mn and N codoped carbon materials are proposed as one of the most promising catalysts for the oxygen reduction reaction (ORR) but still confront a lot of challenges to replace Pt. Herein, a novel gas-phase migration strategy is developed for the scale synthesis of atomically dispersed Mn and N codoped carbon materials (g-SA-Mn) as highly effective ORR catalysts. Porous zeolitic imidazolate frameworks serve as the appropriate support for the trapping and anchoring of Mn-containing gaseous species and the synchronous high-temperature pyrolysis process results in the generation of atomically dispersed Mn-N<sub>x</sub> active sites. Compared to the traditional liquid phase synthesis method, this unique strategy significantly increases the Mn loading and enables homogeneous dispersion of Mn atoms to promote the exposure of Mn-N<sub>x</sub> active sites. The developed g-SA-Mn-900 catalyst exhibits excellent ORR performance in the alkaline media, including a high half-wave potential (0.90 V vs reversible hydrogen electrode), satisfactory durability, and good catalytic selectivity. In the practical application, the Zn–air battery assembled with g-SA-Mn-900 catalysts shows high power density and prominent durability during the discharge process, outperforming the commercial Pt/C benchmark. Such a gas-phase synthetic methodology offers an appealing and instructive guide for the logical synthesis of atomically dispersed catalysts.

density and energy conversion efficiency, abundant Zn sources, and environmental benignity. Oxygen reduction reaction (ORR) at the air cathode plays a critical role in the devices; however, the sluggish kinetics and unsatisfactory stability restrict the electrochemical performance of the Zn–air batteries.<sup>[1]</sup> So far, Pt-based catalysts possess the optimal catalytic capability toward ORR. Nevertheless, the low reserves and exorbitant price of Pt greatly limit their extensive use in practical Zn–air batteries. In addition, Pt-based catalysts exhibit inferior cycling durability and vulnerability to the intermediate by-products in the reaction system.<sup>[2]</sup>

Transition metal and heteroatom codoped carbon materials (M-N-C, M = Fe, Co, Mn, etc.) are identified to be the most hopeful proposition to replace Pt for their unique structure and physicochemical properties.<sup>[3]</sup> Among these heterogeneous catalysts, Fe-N-C catalysts are thought to possess the best catalytic activity toward oxygen reduction, but their stability is still unsatisfactory. Another concern is that

Fe-N-C catalysts may result in Fenton effect (Fe<sup>2+</sup> + H<sub>2</sub>O<sub>2</sub>), where H<sub>2</sub>O<sub>2</sub> originates from the by-products of the oxygen reduction. Alternatively, Mn-N-C catalysts have been reported to exhibit the comparable catalytic capability to Fe-N-C catalysts from

## 1. Introduction

Zn–air batteries are considered as one of the most potential energy storage and conversion devices owing to the satisfactory energy

Q. Y. Zhou, J. J. Cai, Dr. L. Zhao, X. F. Gong, Y. L. Zhang, Dr. X. L. Sui, Prof. Z. B. Wang  
 MIT Key Laboratory of Critical Materials Technology for New Energy Conversion and Storage  
 State Key Lab of Urban Water Resource and Environment  
 School of Chemistry and Chemical Engineering  
 Harbin Institute of Technology  
 Harbin 150001, P. R. China  
 E-mail: leizhao@hit.edu.cn; suixulei@hit.edu.cn; wangzhib@hit.edu.cn

Z. Zhang, Dr. R. Gao, Dr. G. B. Wen, Dr. L. Zhao, Dr. Y. P. Deng, Dr. H. Z. Dou, Prof. A. P. Yu, Prof. Z. W. Chen  
 Department of Chemical Engineering  
 Waterloo Institute for Nanotechnology  
 Waterloo Institute for Sustainable Energy  
 University of Waterloo  
 Waterloo, Ontario N2L 3G1, Canada  
 E-mail: zhwen@uwaterloo.ca

 The ORCID identification number(s) for the author(s) of this article can be found under <https://doi.org/10.1002/smt.202100024>.

Dr. B. Chen  
 Center for Programmable Materials  
 School of Materials Science and Engineering  
 Nanyang Technological University  
 50 Nanyang Avenue, Singapore 639798, Singapore  
 Prof. Y. F. Hu  
 Canadian Light Source  
 University of Saskatchewan  
 Saskatoon, Saskatchewan S7N 0X4, Canada

DOI: 10.1002/smt.202100024

the viewpoint of the density functional theory calculations.<sup>[4]</sup> Besides, Mn-N-C catalysts are free from the persecution of the Fenton effect because of the weak reactivity between Mn and H<sub>2</sub>O<sub>2</sub>. Among the plenty of methods developed to synthesize the Mn-N-C catalysts, high-temperature pyrolysis of transition metal-contained precursor is the most commonly used strategy.<sup>[5]</sup> But the severe agglomeration under high temperature is inevitable because of the thermodynamic properties, heavily damaging the Mn-N<sub>x</sub> active sites.<sup>[6]</sup> Besides, the uniform distribution of the metallic element is also an intractable challenge to be addressed. Postprocessing is another resultful strategy to introduce transition metal to the C-N system, but the repeatedly pyrolysis process leading to the loss of N, and the erratic conjugation of metal center and C/N materials increase the uncertainty of the catalytic performance.<sup>[7]</sup> Different kinds of strategies can be used to carry out the atomic scale doping of metal species, in which guest–host method is one of the effective ways to accomplish the process, for instance, impregnation-adsorption,<sup>[8]</sup> electrolytic deposition,<sup>[9]</sup> atomic layer deposition,<sup>[10]</sup> microwave,<sup>[11]</sup> high temperature shockwave,<sup>[12]</sup> and metal bulk transformation.<sup>[13]</sup> But there are still some shortcomings for these methods, including high-waste cost, low yield, exclusive experiment synthesis condition, or tough requirement. Besides, complicated selection or modification of substrate is also a troublesome portion in these methods. As such, it is urgent and significant for the exploration of facile method for the effective incorporation of metal species and generation of valid active sites.

Herein, we propose a novel gas-phase introducing method to develop an atomically dispersed Mn and N codoped carbon materials (g-SA-Mn) as highly effective catalysts for ORR. The strategy is based on the evaporation of MnCl<sub>2</sub>·4H<sub>2</sub>O under low temperature to serve as Mn source and the following rapid heating process accomplishes the carbonization of Zn-based zeolitic imidazolate frameworks (ZIF-8) accompanied by the generation of atomic Mn-N<sub>x</sub> active sites. This unique strategy not only significantly increases the Mn loading but also enables homogeneous dispersion of Mn atoms throughout the carbon framework to facilitate the exposure of Mn-N<sub>x</sub> active sites. Besides, this in situ pyrolysis process circumvents the unessential mechanical mixing of metal and N-doped carbon support, increasing the number of the effective active sites while maintaining a uniform dispersion.<sup>[14]</sup> Additionally, the synthesis of the catalysts can be easily scaled up at a satisfactory yield. The final catalysts possess a superior specific surface area and interconnected hierarchical pore structure to enable the fast mass transfer and sufficient use of the Mn-N<sub>x</sub> sites. Attributed to these merits, the developed g-SA-Mn-900 catalyst (prepared at 900 °C) exhibits comparable catalytic performances to commercial Pt/C, including the high half-wave potential (0.9 V), efficient four-electron pathway toward ORR and remarkable stability during accelerated aging test (9 mV of half-wave potential offset after 5000 cycles). Besides, the Zn–air battery assembled with the catalysts displays high power density and outstanding stability, suggesting the promise of the catalysts in the practical application.

## 2. Results and Discussion

The schematic illustration for the preparation of g-SA-Mn is shown in **Figure 1**. ZIF-8 was first prepared to be the

precursor of carbon and nitrogen. Afterward, the synthetic ZIF-8 precursor and MnCl<sub>2</sub>·4H<sub>2</sub>O were placed in the tube furnace separately, where MnCl<sub>2</sub>·4H<sub>2</sub>O was placed in upstream to accomplish the doping of manganese into ZIF-8. Then the temperature rapidly rose and remained at 150 °C for the complete volatilization of the MnCl<sub>2</sub>·4H<sub>2</sub>O, whose boiling point is 119 °C. ZIF-8 derived N-doped carbon worked as the host to capture the gaseous Mn species, leading to the atomically dispersed Mn-N<sub>x</sub> active sites during the high-temperature pyrolysis process. After the high temperature carbonization process, the black powder was washed by H<sub>2</sub>SO<sub>4</sub> and subjected to the calcination process again to obtain the final product marked as g-SA-Mn.

The morphology of the materials is first detected by scanning electron microscopy (SEM) and transmission electron microscopy (TEM). The as-prepared ZIF-8 exhibits a distinct dodecahedron facade with the homogeneous diameter of about 130 nm in **Figure S1a** in the Supporting Information. The X-ray diffraction (XRD) pattern of the ZIF-8 shows a favorable matching degree with the simulated ZIF-8, implying the successful synthesis of the pure crystal (**Figure S1b**, Supporting Information). Besides, the sharp peaks of the pattern suggest the high crystallinity degree of the synthetic ZIF-8. **Figure 1a** and **Figure S2** in the Supporting Information clearly display the SEM images of the final catalysts prepared at different pyrolysis temperatures from 700 to 1000 °C. After high-temperature pyrolysis process, the materials still remain the original morphology without apparent breakage, suggesting the stable characteristic of the ZIF-8. The size of the particle changes with a slight decrease with the rising calcination temperature, which is mainly due to the shrinkage of the carbon layer. TEM test was executed to further analyze the structure of the catalysts. **Figure 1b** exhibits that the g-SA-Mn-900 presents well-defined dodecahedral structure without apparent agglomeration of metal nanoparticles, suggesting the prominent dispersity of the Mn element, which could contribute to the increase of Mn-N<sub>x</sub> active sites and the enhancement of the catalytic performance. High-resolution TEM (HR-TEM) image in **Figure 1c** demonstrates the amorphous carbon in g-SA-Mn-900.<sup>[15]</sup> It is widely accepted that the amorphous carbon is inclined to generate defects which contribute to the doping of heteroatoms and generation of active sites, improving the catalytic capability of the catalysts.<sup>[16]</sup> In addition, HR-TEM image also provides compelling evidence for the good dispersion of Mn due to the absence of small-sized nanoparticles at high magnification. In order to precisely identify the dispersity of Mn in the catalyst, high-angle annular dark-field scanning TEM (AC HAADF-STEM) was used as shown in **Figure 1d**. A large amount of circled white dots are detected in the carbon matrix, which is assigned to the highly dispersed Mn atoms. Besides, there are no Mn nanoparticles or clusters appearing in the catalyst, verifying the atomic dispersion of Mn in the sample. STEM image and element mapping in **Figure 1e** reveal the homogeneous dispersion of Mn and N in the carbon matrix. The exact content of Mn in g-SA-Mn-900 is 2.9 wt% according to the inductively coupled plasma (ICP) test, indicating the successful doping of Mn through the efficient and unique gas-transporting strategy.

XRD was first employed to investigate the chemical composition of the materials. The XRD patterns in **Figure 2a**

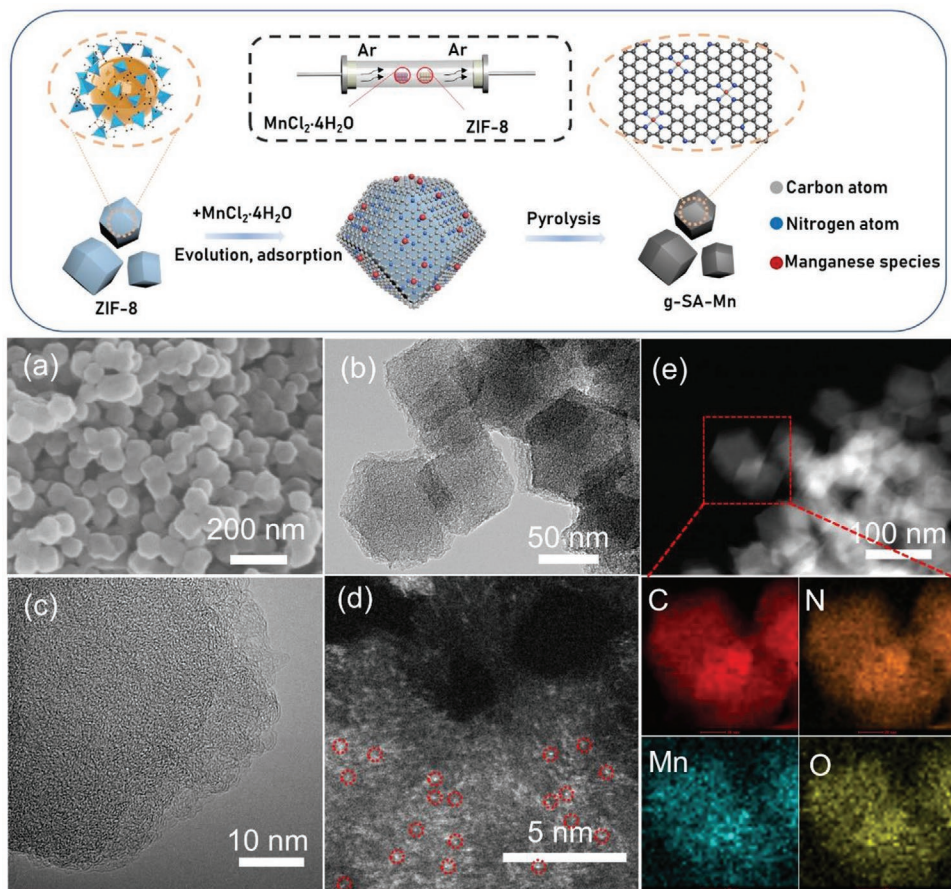


**Figure 1.** Schematic illustration for the preparation of g-SA-Mn and a) SEM image, b) TEM image, c) HR-TEM image, d,e) HADDF-STEM images and corresponding element mapping of g-SA-Mn-900 catalyst.

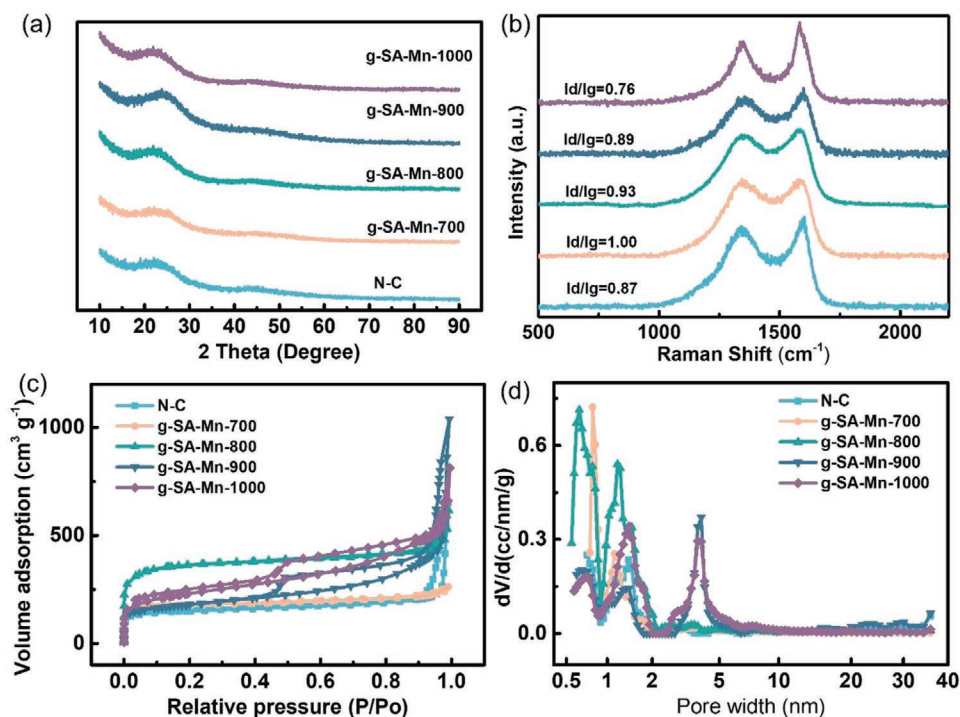


**Figure 2.** a) XRD patterns, b) Raman spectra, c)  $N_2$  adsorption–desorption isotherm, and d) pore size distribution plots for different catalysts.

demonstrate that all the prepared g-SA-Mn catalysts show a (002) lattice plane at around  $24^\circ$  assigned to carbon.<sup>[17]</sup> The detailed insight into the carbon structure and defect of the as-prepared catalysts is accomplished by the Raman spectra. In Figure 2b, the two evident graphitic peaks at 1340 and 1590  $\text{cm}^{-1}$  are identified as the D band and G band of carbon.<sup>[18]</sup> The specific ratio of  $I_D$  to  $I_G$  is a common indicator for the evaluation the disorder degree of the carbon. After the calculation, the  $I_D/I_G$  for g-SA-Mn-X ( $X = 700, 800, 900,$  and  $1000$ ) are 1, 0.93, 0.89, and 0.76, respectively, implying the existence of much defect in the graphitic structure of the catalysts, which is available for the generation of active sites.  $\text{N}_2$  adsorption–desorption experiment was carried out for the analyzation the specific surface area as well as porous structure of the prepared catalysts. Typical type I and IV combinative isotherms are observed in Figure 2c, suggesting the coexistence of microporous and mesoporous hierarchical structure. Specifically, a narrow knee at low pressure with the formation of an adsorption plateau together with the distinct hysteresis loop at the higher pressure region imply the existence of micropore and mesopore, respectively. The specific surface area of N-C and g-SA-Mn-X (700, 800, 900, and 1000  $^\circ\text{C}$ ) are 403, 687, 1360, 819, and 647  $\text{m}^2 \text{g}^{-1}$ , respectively. Additionally, it is well recognized that the ultrahigh pyrolysis temperatures lead to higher degree of graphitization, giving rise to more compact structure of the catalysts as well as slight decline of the specific surface area,<sup>[19]</sup> also accordant to the XRD and Raman results. Pore size distribution reveals that the as-prepared catalysts possess abundant pore at 0.6, 1.2, and 4 nm. Besides, with the raising of calcination temperature, the pore structure of the catalysts turns from the micropore-dominant structure to the mesopore-dominant structure, also being an important factor for the decline of the specific surface area.<sup>[20]</sup> Reasonably optimized porous structure is one of the most crucial factors impacting the catalytic performance of the catalysts, among which mesopore is conducive to the high catalytic performance on account of favorable mass transfer and active sites exposure.

X-ray photoelectron spectroscopy was employed to inspect the chemical component and chemical structure of the catalysts. Figure S3 in the Supporting Information reveals that g-SA-Mn catalysts are comprised by four constituents including C, N, O, and Mn, and the specific ingredient list are displayed in Table S1 in the Supporting Information. Figure 3a and Figure S4 in the Supporting Information demonstrate that C1s spectra can be assigned to C-C (284.6 eV) and C-N (285.4 eV).<sup>[21]</sup> With respect to N1s spectra, there are four species of N exists in the catalysts (Figure 3b and Figure S5, Supporting Information), which are pyridinic N (398.7 eV),<sup>[22]</sup> Mn-N<sub>x</sub> (399.1 eV),<sup>[4b]</sup> pyrrole N (400.3 eV),<sup>[23]</sup> and graphite N (401.5 eV),<sup>[24]</sup> with the contents listed in Table S2 in the Supporting Information. It is obvious that pyridinic N and graphite N possess the predominant status in g-SA-Mn, which is one of the principal factors to promote the catalytic performances.<sup>[25]</sup> Researchers have found that pyridinic N is unstable at high temperature and will convert into quaternary N, leading to the decrease of pyridinic N and augmentation of graphite N.<sup>[25]</sup> The definite effect of pyridinic N and graphite N is still a controversial debate. One of the recognized consequences is that pyridinic N contributes to

the generating of active sites while graphite N is more efficient for the promotion of electrical conductivity of catalysts.<sup>[26]</sup> High-resolution Mn 2p spectra in Figure S6 in the Supporting Information indicates the successful doping of Mn in the catalysts.

According to the aforementioned HR-TEM and XRD results, Mn element has been demonstrated to be highly dispersed in the catalysts, which is necessary to be further investigated by X-ray absorption spectroscopy (XAS). The results of X-ray absorption near edge structure (XANES) spectroscopy and extended X-ray absorption fine structure (EXAFS) spectroscopy for the developed g-SA-Mn-900 and referenced Mn foil and Mn phthalocyanine (Mn-Pc) are present in Figure 3c,d for the further analyzation of the fine structure and chemical coordination environment of the Mn in the catalysts. As Figure 3c shows, the absorption edge of g-SA-Mn-900 is between that of Mn-foil and Mn-Pc, indicating the Mn valence state in the catalysts is between Mn foil and Mn-Pc. The distinction of g-SA-Mn-900 and Mn foil in near-edge is mainly due to the different chemical environment of Mn atoms in the prepared g-SA-Mn-900 catalyst and Mn foil.<sup>[27]</sup> The strong interaction of Mn atoms to N and C atoms in g-SA-Mn-900 and Mn-Pc could lead to the obvious positive shift compared to Mn foil, suggesting that Mn possesses higher oxidation state in g-SA-Mn-900 and Mn-Pc. This phenomenon can also be verified by the Fourier transformation result of Mn K-edge EXAFS data. As shown in Figure 3d, the mainly peak at 1.46 Å corresponds to the Mn-N binding, which is the dominant coordination environment for Mn in the catalysts. Besides, the peak at 2.3 Å due to Mn-Mn interaction does not appear in g-SA-Mn-900, further affirming the absence of Mn clusters in the catalysts.<sup>[4a,b,8]</sup> Based on the EXAFS spectrum of g-SA-Mn-900, the expectant refined structure in the catalyst is well fitted with Mn-N<sub>4</sub> coordination, meaning that one Mn atom coordinates with four N atoms, which serves as the dominated active site for ORR (Figure S7 and Table S3, Supporting Information). The wavelet transform (WT) results in Figure 3e,f present only one intensity maximum at around 4  $\text{\AA}^{-1}$  in g-SA-Mn-900 catalysts, further suggesting the absence of Mn cluster in the catalyst.

The electrochemical property of g-SA-Mn catalysts was appraised to elaborate the advantages of the compositions and chemical structure toward electrocatalysis. First of all, cyclic voltammetry (CV) was used to investigate the catalytic capability of g-SA-Mn-900 by recording the curves in O<sub>2</sub> or N<sub>2</sub>-saturated 0.1 mol L<sup>-1</sup> potassium hydroxide (KOH) electrolyte, as present in Figure 4a. There is no distinct peak existing according to the curve in N<sub>2</sub>-saturated electrolyte, suggesting no electrochemical reaction occurred during the test. A marked redox peak at 0.83 V (vs reversible hydrogen potential) appears in O<sub>2</sub>-saturated KOH, which corresponds to the oxygen reduction reaction, implying the remarkable ORR catalytic ability of the catalyst.

The optimal pyrolysis temperature for the g-SA-Mn is 900  $^\circ\text{C}$  is illustrated in Figure 4b. The four catalysts present the half-wave potential of 0.70, 0.82, 0.90, and 0.84 V as the pyrolysis temperature raises from 700 to 1000  $^\circ\text{C}$ . Higher pyrolysis temperature not only leads to higher degree of graphitization that improves the electrical conductivity of the catalysts but also tunes the entire content and fine composition of N.<sup>[28]</sup> To further illustrate the reaction kinetics and electrochemical performance of the g-SA-Mn, l-Mn-N, N-C, and commercial Pt/C

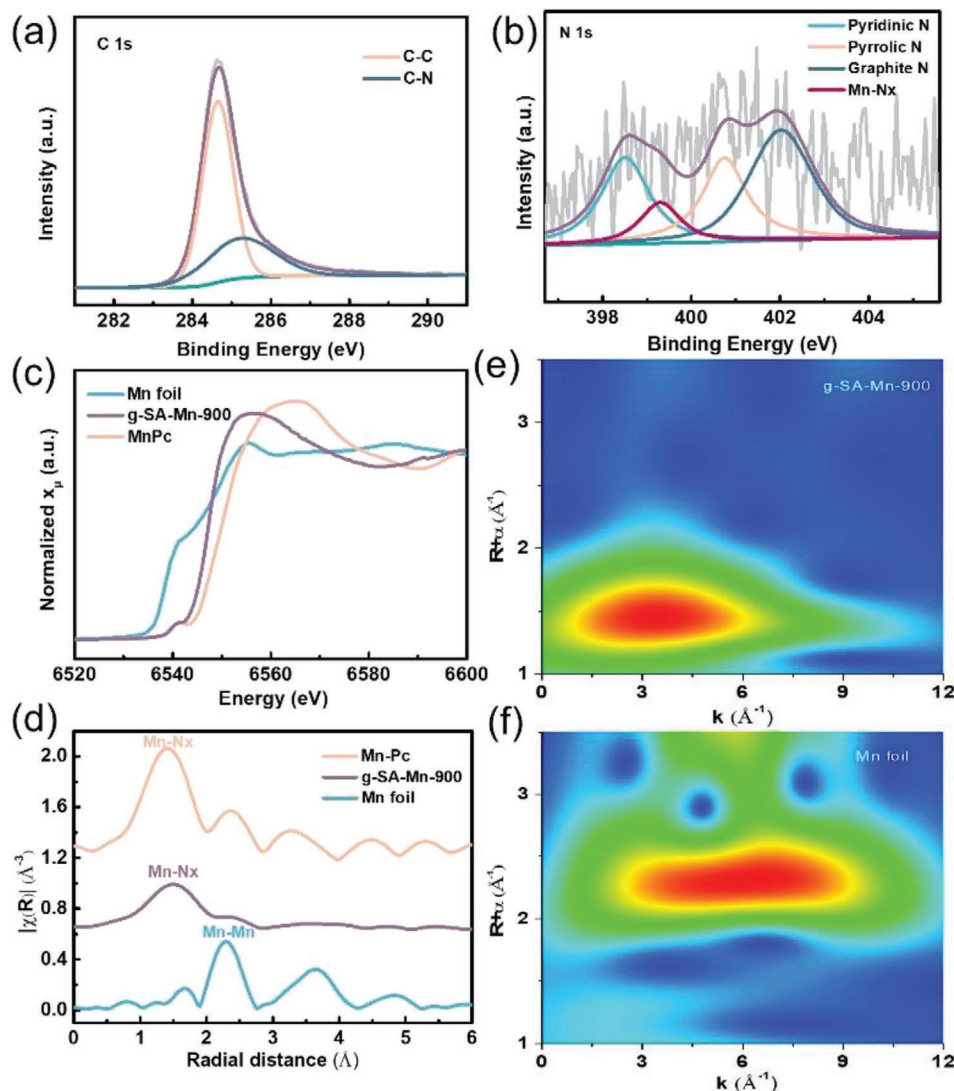


**Figure 3.** High-resolution a) C1s and b) N1s peaks of g-SA-Mn-900. c) K-edge XANES spectra for g-SA-Mn-900, Mn foil, and MnPc. d) Fourier transforms of Mn K-edge EXAFS data for g-SA-Mn-900, Mn foil, and MnPc. WT of experimental EXAFS of e) g-SA-Mn-900 and f) Mn foil.

catalysts, rotating ring-disk electrode (RRDE) test was performed in  $O_2$ -saturated  $0.1 \text{ mol L}^{-1}$  KOH electrolyte at 1600 rpm. Staircase voltammetry (SCV) curves for the catalysts can be seen in Figure 4c. g-SA-Mn displays much better ORR performance than l-Mn-N and N-C in terms of highest half-wave potential (0.90 V) and largest limiting current density ( $5.8 \text{ mA cm}^{-2}$ ). ICP test reveals the content of Mn in l-Mn-N, g-SA-Mn-900 is 1.1% and 2.9%, respectively, indicating the valid introduction of Mn through gas-phase introducing strategy. As expected, g-SA-Mn indeed exhibits comparable ORR activity to commercial Pt/C (0.90 V), implying the remarkable performance of the catalysts. Figure 4d exhibits the  $HO_2^-$  yield ( $\%HO_2^-$ ) and electron transfer number ( $n$ ) of g-SA-Mn, N-C and Pt/C, where g-SA-Mn shows a  $\%HO_2^-$  below 10% with the potential ranging from 0.2 to 0.8 V, which is comparative to Pt/C and much lower than N-C. Besides, the value of  $n$  for g-SA-Mn is 3.8–3.9, signifying that g-SA-Mn primary catalyzes the reduction of  $O_2$  through a desirable four-electron pathway.<sup>[29]</sup> By contrast, N-C presents the  $n$  of 3.5, which is

much lower than g-SA-Mn, implying a mixture of two- and four-electron pathway. These results clearly demonstrate the pivotal role of the Mn-doping within the C-N framework in enhancing the ORR catalytic performance of g-SA-Mn catalysts. For the in-depth insight of kinetics toward ORR, the value of  $n$  can also be calculated by K-L equation<sup>[30]</sup> As shown in Figure 4e, the  $n$  is calculated to be 3.8 according to the SCV curves at different rotating speeds, being highly accordant with the RRDE result, further confirming the expedited four-electron reaction pathway for ORR.

The durability of the g-SA-Mn is first inspected by current–time ( $i-t$ ) chronoamperometric responses at 0.8 V with the rotational speed of 1600 rpm as shown in Figure 4f. After 10 000 s test, g-SA-Mn shows a 9% loss of the current, showing a much less decay than the Pt/C (21%), indicating the remarkable stability during the continual reaction. In order to check the long-time stability of the catalysts, SCV curves are recorded before and after 5000 cycle between 0.6 and 1.0 V, as shown in Figure 4g and Figure S8 in the Supporting Information.

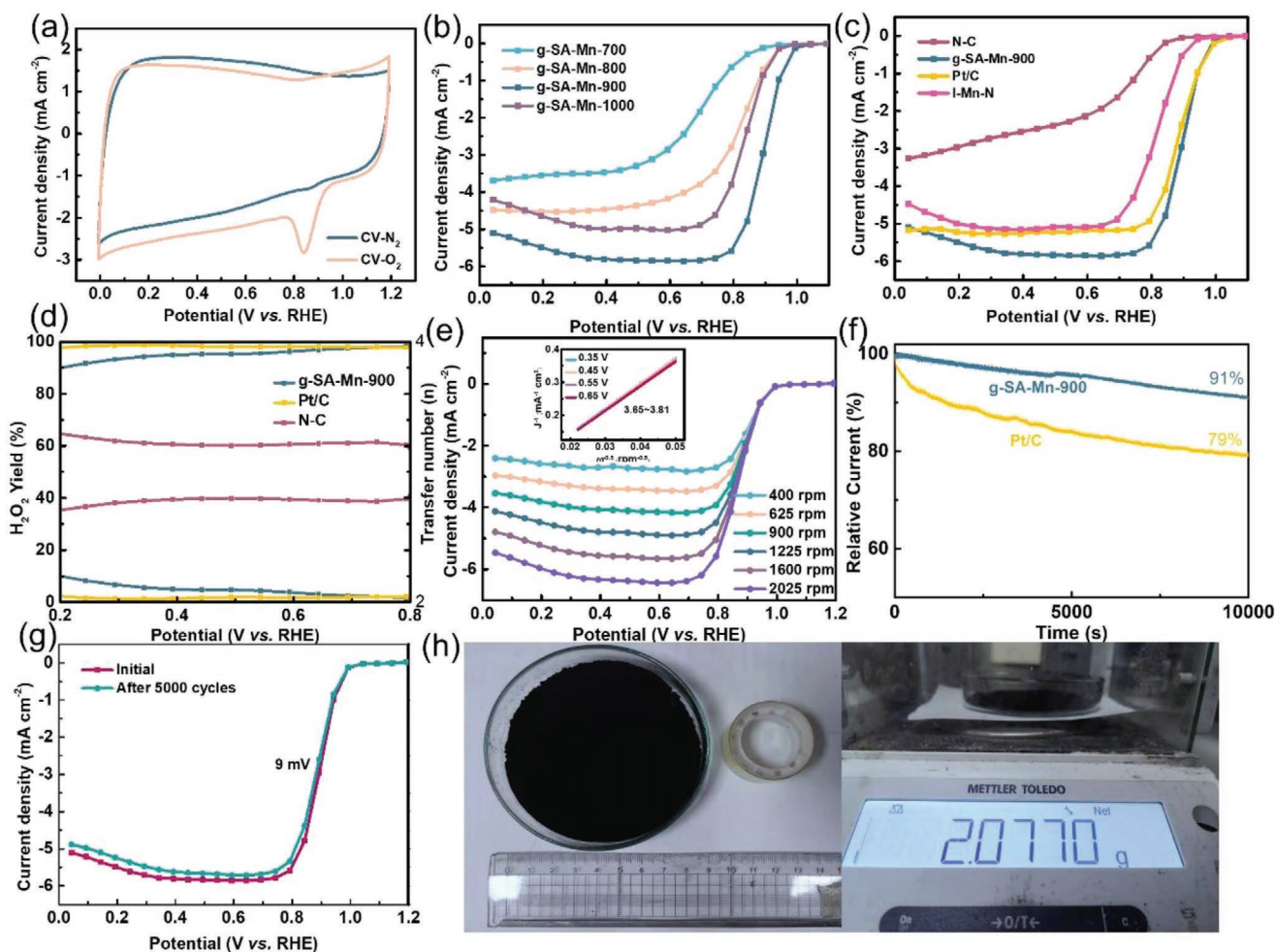


**Figure 4.** a) CV curves for g-SA-Mn-900 in  $N_2$  or  $O_2$ -saturated  $0.1 \text{ mol L}^{-1}$  KOH. b) SCV curves of the catalysts with various pyrolysis temperature in  $O_2$ -saturated  $0.1 \text{ mol L}^{-1}$  KOH at 1600 rpm. c) SCV curves of N-C, g-SA-Mn-900, I-Mn-N, and Pt/C at 1600 rpm. d)  $H_2O_2$  yield and transfer number according to the RRDE test. e) Polarization curves of g-SA-Mn-900 at different rotate speed and f) linear fitting plots according to K–L equation (inset). f) The chronoamperometric curves of g-SA-Mn-900 and Pt/C at 0.8 V with the rotation speed 1600 rpm. g) SCV curves for g-SA-Mn-900 at 1600 rpm before and after 5000 cycles accelerated aging test from 0.6 to 1.0 V at  $50 \text{ mV s}^{-1}$ . h) Digital photograph of the high yield g-SA-Mn-900 catalysts.

g-SA-Mn presents far less negative shift of half-wave potential than Pt/C (9 mV vs 23 mV), indicative of its much better long-term stability. The ability to bear the poison effect of methanol is another pregnant evaluation for ORR catalysts in case the catalysts exhibit extremely sensitive character to the intermediate products and impurity.<sup>[31]</sup> As shown in Figure S9 in the Supporting Information, Pt/C reveals distinct catalytic capability to methanol oxidation according to the apparent peaks attributed to the oxidation of methanol. By contrast, g-SA-Mn possesses almost the same polarization curves after the addition of methanol, indicating the particular selectivity of the catalyst. As reported, the small difference of adsorption energies calculated for oxygen and methanol on Pt (111) surface leading to the inferior tolerance of Pt catalyst to methanol poisoning. While the adsorption energies for oxygen on M-N<sub>x</sub> (M = Fe, Co, Ni) sites are usually much larger than that of methanol, which brings about the high tolerance to methanol poisoning and good selectivity to ORR.<sup>[32]</sup> In addition, the catalysts can be facilely synthesized at a large scale with a high yield as shown in Figure 4h.

In order to investigate the practical application of our g-SA-Mn-900 catalysts, Zn–air batteries were assembled with g-SA-Mn-900 and Pt/C catalysts as air-cathode, respectively. The open-circuit potential of the battery is 1.442 V (Figure 5a). Figure 5b presents that the battery with g-SA-Mn-900 catalysts demonstrates higher voltage than Pt/C. Moreover, power density curves display that the battery with g-SA-Mn-900 exhibits the maximum power density of  $147 \text{ mW cm}^{-2}$  at  $214 \text{ mA cm}^{-2}$ , higher than that with Pt/C ( $133 \text{ mW cm}^{-2}$  at  $183 \text{ mA cm}^{-2}$ ). As the satisfactory ORR durability of the g-SA-Mn-900 catalyst has been confirmed in the above results, we execute a long-time galvanostatic discharge test at  $10 \text{ mA cm}^{-2}$  to further verify the stability of the Zn–air batteries. As present in Figure S10 in the Supporting Information, the two batteries both exhibit acceptable durability in the test. To be specific, the battery with g-SA-Mn-900 catalysts possesses the voltage loss of 34 mV after 120 h operation, which is less than the other with Pt/C benchmark of 53 mV. This test output the same result as the electrochemistry test, further verifying the optimized stability of our

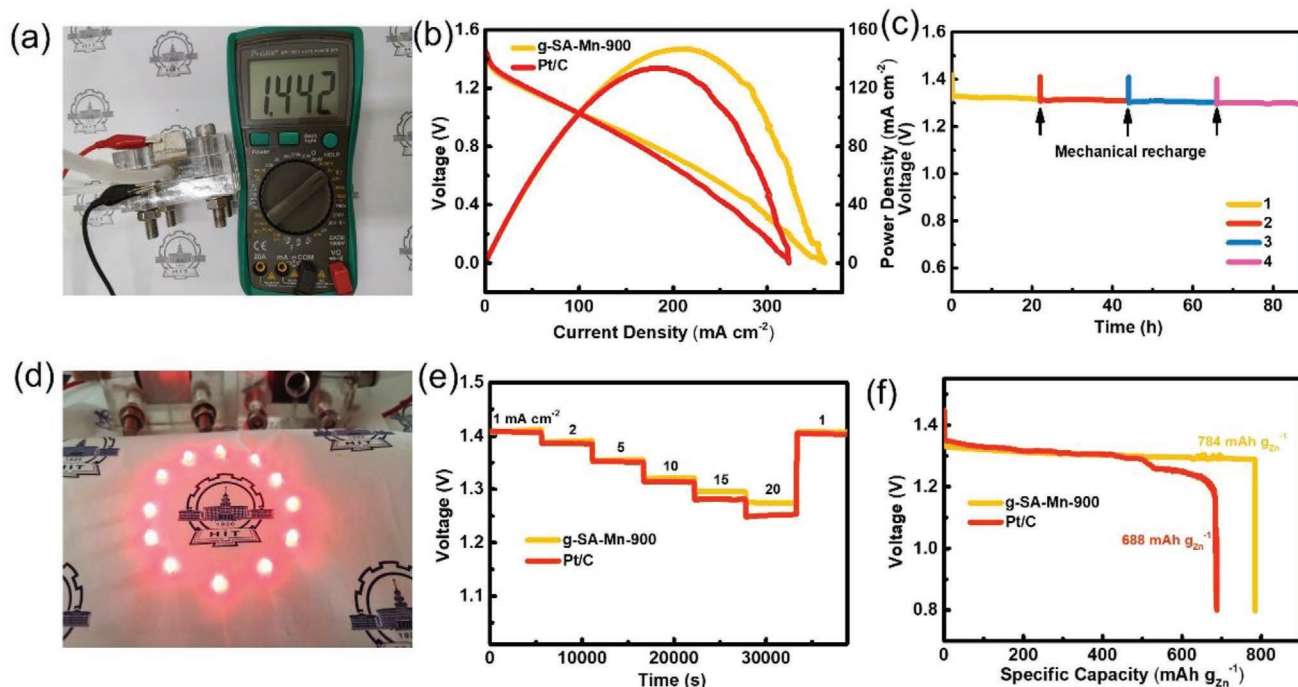


**Figure 5.** a) Open-circuit of the Zn–air battery with g-SA-Mn-900 catalyst, b) galvanostatic discharge voltage and power density curves of the Zn–air batteries with g-SA-Mn-900 and Pt/C catalysts. c) Lifetime test of the Zn–air battery with g-SA-Mn-900 by recharging Zn anode after galvanostatic discharge at  $10 \text{ mA cm}^{-2}$ . d) Practical lighting test for the Zn–air battery with g-SA-Mn-900 catalyst. e) Rate capability test of the Zn–air batteries with g-SA-Mn-900 and Pt/C catalysts at different current densities. f) Specific capacity using the Zn–air battery with g-SA-Mn-900 and Pt/C catalysts.

g-SA-Mn-900 than Pt/C. Additionally, the lifetime of the battery with g-SA-Mn-900 catalyst are also studied by recharging Zn anode after 22 h galvanostatic discharge at  $10 \text{ mA cm}^{-2}$ . Figure 5c indicates that the battery can be continuously operated for over 80 h without evident voltage loss after four-time renewal of the Zn anode. In order to check the possibility in practical applications, two batteries are connected in series to lighten the 16 light emitting diode lights in Figure 5d. Also, the rate capability of the two batteries was inspected by changing the discharge current density between 1 and  $20 \text{ mA cm}^{-2}$  to meet the discharging requirement at various current densities which is present in Figure 5e. Comparing to Pt/C, the Zn–air battery with g-SA-Mn-900 catalysts presents higher voltage platform at the same discharge current density, indicating better rate capability of g-SA-Mn-900 than commercial Pt/C. The specific capacity of the battery with g-SA-Mn-900 and Pt/C catalyst are calculated to be 784 and  $688 \text{ mAh g}_{\text{Zn}}^{-1}$  shown in Figure 5f. In order to objectively appraise the obtained g-SA-Mn-900 catalyst, some catalysts in previous reference are listed in Table S4 in the Supporting Information, further indicating the potential of g-SA-Mn-900 catalyst.

### 3. Conclusion

In conclusion, we developed a novel gas phase introducing method to scale synthesize atomically dispersed Mn and N codoped carbon catalysts (g-SA-Mn) for ORR.  $\text{MnCl}_2 \cdot 4\text{H}_2\text{O}$  works as the volatile Mn precursor while porous ZIF-8 serves as the substrate to trap and anchor gaseous Mn-containing species

and finally convert into atomically dispersed  $\text{Mn-N}_x$  active sites catalysts after the high-temperature calcination process. This novel strategy achieves the homogeneous dispersion of Mn atoms and conspicuously increases the Mn loading throughout the carbon framework to promote the exposure of  $\text{Mn-N}_x$  active sites. Additionally, it is facile to accomplish the scale up production of the catalysts with a high yield. The obtained g-SA-Mn-900 catalysts exhibit intrinsic single-atom  $\text{Mn-N}_x$  active centers and greatly promoted accessibility through optimized specific surface area, pore structure, elemental component, and state by thermal activation. The characteristic structure endows the catalysts with favorable catalytic capability toward ORR, including high half-wave potential, four electron pathway, good durability, and excellent tolerance to methanol. Zn–air battery assembled with g-SA-Mn-900 catalysts shows high power density and favorable stability during the discharge process, suggesting the potential of our catalysts in the practical application.

### 4. Experimental Section

**Synthesis of ZIF-8 Precursor:** 5.9 g  $\text{Zn}(\text{NO}_3)_2 \cdot 6\text{H}_2\text{O}$  and 6.57 g 2-methylimidazole were dissolved in 300 mL methanol, respectively. White sediment was obtained after the mixing of the two solutions by 2 h stirring following by standing for 22 h. The product was collected by centrifuge, washed by methanol for three times, and dried at  $80 \text{ }^\circ\text{C}$  for 6 h in oven.

**Synthesis of g-SA-Mn, N-C, and I-Mn-N:** 300 mg ZIF-8 and 500 mg  $\text{MnCl}_2 \cdot 4\text{H}_2\text{O}$  were placed in two independent boats and put into the tube furnace with flowing Ar atmosphere. Then the boats were heated at  $150 \text{ }^\circ\text{C}$  for 1 h and various temperature ( $700\text{--}1000 \text{ }^\circ\text{C}$ ) for 2 h a ramping rate of  $20 \text{ }^\circ\text{C min}^{-1}$ . The product was then disposed by  $0.5 \text{ mol L}^{-1} \text{ H}_2\text{SO}_4$ ,

washed by deionized water, and drying in the oven. Finally, g-SA-Mn was obtained after the calcination of dried powder in a tube furnace at the same temperature for 2 h under Ar atmosphere. N-C was prepared by the simple calcination of ZIF-8 under the same condition. Mn-ZIF was synthesized similar to ZIF-8 except that 20%  $\text{MnCl}_2 \cdot 4\text{H}_2\text{O}$  was added to replace  $\text{Zn}(\text{NO}_3)_2 \cdot 6\text{H}_2\text{O}$ . Afterward the dried powder was heated at 900 °C in tube furnace to obtain the control sample named as I-Mn-N.

**Characterization:** XRD, SEM, TEM, XAS, and more measurement were employed to detect the physical properties. The electrochemical measurements were carried out in a standard three-electrode system. CV, SCV, and some other test were executed to inspect the electrocatalytic capability of catalysts. The specific parameters are listed in the Supporting Information.

## Supporting Information

Supporting Information is available from the Wiley Online Library or from the author.

## Acknowledgements

Q.Y.Z., J.J.C., and Z.Z. contributed equally to this work. The authors acknowledge the National Natural Science Foundation of China (Grant Nos. 21673064, 51802059, 21905070, 22075062, and U1909213), China postdoctoral science foundation (Grant Nos. 2017M621284, 2018M631938, and 2018T110307), Heilongjiang Postdoctoral Fund (LBH-Z17074 and LBH-Z18066) and Fundamental Research Funds for the Central Universities (Grant Nos. HIT.NSRIF.2019040 and 2019041), the Natural Sciences and Engineering Research Council of Canada (NSERC), University of Waterloo, and Waterloo Institute for Nanotechnology. The authors also thank Dr. Qunfeng Xiao from soft X-ray microcharacterization beamline (SXRMB) of Canadian Light Source (CLS) for XAS measurements. The CLS was supported by the NSERC, the National Research Council Canada, the Canadian Institutes of Health Research, the Province of Saskatchewan, Western Economic Diversification Canada, and the University of Saskatchewan.

## Conflict of Interest

The authors declare no conflict of interest.

## Data Availability Statement

Research data are not shared.

## Keywords

atomically dispersed Mn-N<sub>4</sub> sites, gas-phase migration, oxygen reduction reaction, Zn-air batteries

Received: January 8, 2021  
Revised: February 27, 2021  
Published online: April 22, 2021

- [1] a) X. X. Wang, M. T. Swihart, G. Wu, *Nat. Catal.* **2019**, *2*, 578; b) Y. Li, Y. Sun, Y. Qin, W. Zhang, L. Wang, M. Luo, H. Yang, S. Guo, *Adv. Energy Mater.* **2020**, *10*, 1903120.  
[2] a) M. Luo, Z. Zhao, Y. Zhang, Y. Sun, Y. Xing, F. Lv, Y. Yang, X. Zhang, S. Hwang, Y. Qin, J. Y. Ma, F. Lin, D. Su, G. Lu, S. Guo,

- Nature* **2019**, *574*, 81; b) M. Qiao, Y. Wang, Q. Wang, G. Hu, X. Mamat, S. Zhang, S. Wang, *Angew. Chem., Int. Ed. Engl.* **2020**, *59*, 2688.  
[3] T. Najam, S. S. A. Shah, W. Ding, J. Jiang, L. Jia, W. Yao, L. Li, Z. Wei, *Angew. Chem., Int. Ed. Engl.* **2018**, *57*, 15101.  
[4] a) K. Liu, Z. Qiao, S. Hwang, Z. Liu, H. Zhang, D. Su, H. Xu, G. Wu, G. Wang, *Appl. Catal., B* **2019**, *243*, 195; b) L. Bai, Z. Duan, X. Wen, R. Si, J. Guan, *Appl. Catal., B* **2019**, *257*, 117930; c) M. Chen, X. Li, F. Yang, B. Li, T. Stracensky, S. Karakalos, S. Mukerjee, Q. Jia, D. Su, G. Wang, G. Wu, H. Xu, *ACS Catal.* **2020**, *10*, 10523.  
[5] a) B. Lv, S. Zeng, W. Yang, J. Qiao, C. Zhang, C. Zhu, M. Chen, J. Di, Q. Li, *J. Energy Chem.* **2019**, *38*, 170; b) J. Li, S. Chen, N. Yang, M. Deng, S. Ibraheem, J. Deng, J. Li, L. Li, Z. Wei, *Angew. Chem., Int. Ed. Engl.* **2019**, *58*, 7035.  
[6] X. Zhang, X. Han, Z. Jiang, J. Xu, L. Chen, Y. Xue, A. Nie, Z. Xie, Q. Kuang, L. Zheng, *Nano Energy* **2020**, *71*, 104547.  
[7] a) J. Yang, Z. Qiu, C. Zhao, W. Wei, W. Chen, Z. Li, Y. Qu, J. Dong, J. Luo, Z. Li, Y. Wu, *Angew. Chem., Int. Ed. Engl.* **2018**, *57*, 14095; b) P. Yu, L. Wang, F. Sun, Y. Xie, X. Liu, J. Ma, X. Wang, C. Tian, J. Li, H. Fu, *Adv. Mater.* **2019**, *31*, 1901666.  
[8] J. Li, M. Chen, D. A. Cullen, S. Hwang, M. Wang, B. Li, K. Liu, S. Karakalos, M. Lucero, H. Zhang, C. Lei, H. Xu, G. E. Sterbinsky, Z. Feng, D. Su, K. L. More, G. Wang, Z. Wang, G. Wu, *Nat. Catal.* **2018**, *1*, 935.  
[9] Z. Zhang, C. Feng, C. Liu, M. Zuo, L. Qin, X. Yan, Y. Xing, H. Li, R. Si, S. Zhou, J. Zeng, *Nat. Commun.* **2020**, *11*, 1215.  
[10] S. Liu, J. M. Tan, A. Gulec, L. A. Crosby, T. L. Drake, N. M. Schweitzer, M. Delferro, L. D. Marks, T. J. Marks, P. C. Stair, *Organometallics* **2017**, *36*, 818.  
[11] H. Fei, J. Dong, C. Wan, Z. Zhao, X. Xu, Z. Lin, Y. Wang, H. Liu, K. Zang, J. Luo, S. Zhao, W. Hu, W. Yan, I. Shakir, Y. Huang, X. Duan, *Adv. Mater.* **2018**, *30*, 1802146.  
[12] Y. Yao, Z. Huang, P. Xie, L. Wu, L. Ma, T. Li, Z. Pang, M. Jiao, Z. Liang, J. Gao, Y. He, D. J. Kline, M. R. Zachariah, C. Wang, J. Lu, T. Wu, T. Li, C. Wang, R. Shahbazian-Yassar, L. Hu, *Nat. Nanotechnol.* **2019**, *14*, 851.  
[13] Y. Qu, Z. Li, W. Chen, Y. Lin, T. Yuan, Z. Yang, C. Zhao, J. Wang, C. Zhao, X. Wang, F. Zhou, Z. Zhuang, Y. Wu, Y. Li, *Nat. Catal.* **2018**, *1*, 781.  
[14] Z. Yang, C. Zhao, Y. Qu, H. Zhou, F. Zhou, J. Wang, Y. Wu, Y. Li, *Adv. Mater.* **2019**, *31*, 1808043.  
[15] J.-J. Cai, Q.-Y. Zhou, B. Liu, X.-F. Gong, Y.-L. Zhang, K. Goh, D.-M. Gu, L. Zhao, X.-L. Sui, Z.-B. Wang, *Nanoscale* **2020**, *12*, 973.  
[16] X. Yan, Y. Jia, J. Chen, Z. Zhu, X. Yao, *Adv. Mater.* **2016**, *28*, 8771.  
[17] Q. Y. Zhou, L. Zhao, X. L. Sui, X. F. Gong, J. Z. Li, X. F. Li, Z. B. Wang, *Chem. - Asian J.* **2018**, *13*, 3057.  
[18] a) L. Yang, D. Wang, Y. Lv, D. Cao, *Carbon* **2019**, *144*, 8; b) Z. Zhang, Y. P. Deng, Z. Xing, D. Luo, S. Sy, Z. P. Cano, G. Liu, Y. Jiang, Z. Chen, *ACS Nano* **2019**, *13*, 7062; c) H. Luo, B. Wang, F. Wang, J. Yang, F. Wu, Y. Ning, Y. Zhou, D. Wang, H. Liu, S. Dou, *ACS Nano* **2020**, *14*, 7328.  
[19] Y. Niu, X. Huang, X. Wu, L. Zhao, W. Hu, C. Ming Li, *Nanoscale* **2017**, *9*, 10233.  
[20] H. X. Zhong, J. Wang, Y. W. Zhang, W. L. Xu, W. Xing, D. Xu, Y. F. Zhang, X. B. Zhang, *Angew. Chem., Int. Ed. Engl.* **2014**, *53*, 14235.  
[21] a) Q. Niu, K. Gao, Q. Tang, L. Wang, L. Han, H. Fang, Y. Zhang, S. Wang, L. Wang, *Carbon* **2017**, *123*, 290; b) J. Wei, Y. Hu, Y. Liang, B. Kong, Z. Zheng, J. Zhang, S. P. Jiang, Y. Zhao, H. Wang, *J. Mater. Chem. A* **2017**, *5*, 10182; c) H. Luo, B. Wang, C. Wang, F. Wu, F. Jin, B. Cong, Y. Ning, Y. Zhou, D. Wang, H. Liu, S. Dou, *Energy Storage Mater.* **2020**, *33*, 390.

- [22] a) R. Ma, Y. Zhou, C. Hu, M. Yang, F. Wang, K. Yan, Q. Liu, J. Wang, *Energy Storage Mater.* **2018**, *13*, 142; b) Y. Zhang, L.-B. Huang, W.-J. Jiang, X. Zhang, Y.-Y. Chen, Z. Wei, L.-J. Wan, J.-S. Hu, *J. Mater. Chem. A* **2016**, *4*, 7781.
- [23] a) Y. Li, Y. Liu, Q. Qian, G. Wang, G. Zhang, *Energy Storage Mater.* **2020**, *28*, 27; b) X. Chen, Z. Yan, M. Yu, H. Sun, F. Liu, Q. Zhang, F. Cheng, J. Chen, *J. Mater. Chem. A* **2019**, *7*, 24868.
- [24] a) D. Ji, S. Peng, J. Lu, L. Li, S. Yang, G. Yang, X. Qin, M. Srinivasan, S. Ramakrishna, *J. Mater. Chem. A* **2017**, *5*, 7507; b) J. Li, S. Chen, W. Li, R. Wu, S. Ibraheem, J. Li, W. Ding, L. Li, Z. Wei, *J. Mater. Chem. A* **2018**, *6*, 15504.
- [25] L. Zhao, X.-L. Sui, Q.-Y. Zhou, J.-Z. Li, J.-J. Zhang, G.-S. Huang, Z.-B. Wang, *J. Mater. Chem. A* **2018**, *6*, 6212.
- [26] a) D. Guo, R. Shibuya, C. Akiba, S. Saji, T. Kondo, J. Nakamura, *Science* **2016**, *351*, 361; b) Y. He, X. Han, Y. Du, B. Song, P. Xu, B. Zhang, *ACS Appl. Mater. Interfaces* **2016**, *8*, 3601.
- [27] a) Z. Lin, H. Huang, L. Cheng, Y. Yang, R. Zhang, Q. Chen, *ACS Sustainable Chem. Eng.* **2019**, *8*, 427; b) Y. Yang, K. Mao, S. Gao, H. Huang, G. Xia, Z. Lin, P. Jiang, C. Wang, H. Wang, Q. Chen, *Adv. Mater.* **2018**, *30*, 1801732.
- [28] H. Shang, W. Sun, R. Sui, J. Pei, L. Zheng, J. Dong, Z. Jiang, D. Zhou, Z. Zhuang, W. Chen, J. Zhang, D. Wang, Y. Li, *Nano Lett.* **2020**, *20*, 5443.
- [29] Y. Yan, Y. Xu, B. Zhao, Y. Xu, Y. Gao, G. Chen, W. Wang, B. Y. Xia, *J. Mater. Chem. A* **2020**, *8*, 5070.
- [30] Q. Zhou, Z. Zhang, J. Cai, B. Liu, Y. Zhang, X. Gong, X. Sui, A. Yu, L. Zhao, Z. Wang, Z. Chen, *Nano Energy* **2020**, *71*, 104592.
- [31] J. Huang, J. Han, T. Gao, X. Zhang, J. Li, Z. Li, P. Xu, B. Song, *Carbon* **2017**, *124*, 34.
- [32] D. Sebastián, A. Serov, I. Matanovic, K. Artyushkova, P. Atanassov, A. S. Aricò, V. Baglio, *Nano Energy* **2017**, *34*, 195.